Nanoscale

PAPER

Published on 26 October 2026
Licence and permissions

Check for updates

Cite this: DOI: 10.1039/d6nr03055f

Boosting whole-process CO_2 capture *via* dual-pathway synergy by spatially hierarchical sites on carbon-based nanomaterials

Mengcheng Zhan,[a,b] Jingwen Jiang,[a,b] Tingting Xia,[a,b] Jichao Hu,[a] Weiping Zhang,[c] *[c] Dong Xu,*[d] Yulong Wang,[d] Bingyuan Zeng,[a] Baohui Li,[a] Dong Fu[a,b] and Kun Zhao *[a,b]

To address the demand for energy-efficient and scalable CO_2 capture catalysts, we construct a spatially hierarchically functional interface on a carbon-based support, comprising $-SO_3H$ and SiO_x-OH sites. This design exploits their distinct acid strengths and thermal responses: at low temperatures, Si–OH networks facilitate CO_2 uptake *via* proton pre-organization and intermediate stabilization; at elevated temperatures, $-SO_3H$ sites drive C–N bond cleavage and rapid CO_2 release. The spatial proximity of the two sites creates a proton-relay channel, enabling sequential activation with progressively reduced energy barriers. *In situ* FT-IR and DFT calculations reveal that HCO_3^- replaces $MEACOO^-$ as the dominant interfacial desorption intermediate, establishing a dual-pathway mechanism that reduces the thermodynamic penalty of conventional amine regeneration. Under simulated industrial conditions, the optimized catalyst achieves 36.3% desorption efficiency and 39.6% energy savings *versus* the blank, with excellent stability over five cycles. This work provides a theoretical and material foundation for integrating catalytic desorption into amine-based CO_2 capture systems.

Received 7th August 2026,
Accepted 18th September 2026

DOI: 10.1039/d6nr03055f

rsc.li/nanoscale

1. Introduction

The large-scale deployment of carbon capture technologies is widely regarded as a key pathway for mitigating anthropogenic CO_2 emissions.[1–3] Among the various technical routes, the CO_2 capture process based on amine absorption remains the most mature option owing to its high capture efficiency and good industrial applicability.[4,5] However, this process encounters a significant energy consumption bottleneck during the solvent regeneration stage, which mainly originates from the thermal decomposition of carbamates and the restructuring of the hydrogen-bond network in the aqueous solution.[6,7] It has been estimated that the energy consumption for regeneration can account for 60–80% of the total operating cost of the entire capture process.[8,9] Reducing the energy penalty of regeneration is therefore a central challenge for advancing the industrialization and large-scale deployment of this technology.[10,11]

Unlike conventional thermal regeneration methods, solid acid catalysts accelerate interfacial proton transfer and reduce the activation energy for carbamate decomposition by introducing abundant Brønsted (B) and Lewis (L) acid active sites, thereby achieving efficient CO_2 desorption at lower temperatures.[12,13] Extensive studies have confirmed that rationally designed solid acid systems can reduce the regeneration heat duty of amine solvents by 10%–57%.[14] Current research has extensively explored various catalytic material systems: metal-modified ZSM-5 zeolites construct coupled B/L acid centers to synergistically promote proton migration and C–N bond cleavage in carbamates;[13] sulfonic acid-functionalized mesoporous MCM-41 effectively reduces the thermal regeneration load of monoethanolamine (MEA) solvents owing to its abundant acid sites;[15] and sulfonic acid catalysts supported on covalent organic frameworks (COFs) enhance the CO_2 desorption rate by 733% and reduce regeneration energy consumption by 28.8% by optimizing interfacial proton transfer behavior.[16,17] Furthermore, heteropoly acid-modified silica nanospheres, $NiSO_4/NiO$ solid superacids, and MOF-derived Fe_3O_4@C/SiO_2 composites have been demonstrated to enhance the desorption process through unique proton relay

[a]*Hebei Key Lab of Power Plant Flue Gas Multi-Pollutants Control, Department of Environmental Science and Engineering, North China Electric Power University, Baoding, 071003, China. E-mail: zhaokun@ncepu.edu.cn*
[b]*Yanzhao Electric Power Laboratory of North China Electric Power University, Baoding, 071003, China*
[c]*Guangdong Key Laboratory of Environmental Catalysis and Health Risk Control, Guangdong-Hong Kong-Macao Joint Laboratory for Contaminants Exposure and Health, Institute of Environmental Health and Pollution Control, Guangdong University of Technology, Guangzhou 510006, China. E-mail: wp.zhang86@gdut.edu.cn*
[d]*Beijing Key Laboratory of Power Generation System Functional Material, CHN Energy New Energy Technology Research Institute Ltd, Beijing 102209, China. E-mail: 12000185@ceic.com*

and proton-coupled electron transfer (PCET) mechanisms, fully demonstrating the significant potential of solid acid catalysis in energy-efficient carbon capture.[18–20]

Significant cognitive limitations persist in the design of existing catalysts. Most studies treat the catalytic surface as a spatially averaged/bulk-averaged design, using only total acidity and the Brønsted/Lewis (B/L) acid ratio as optimization metrics.[11] For instance, the B/L acid ratio and mesoporous surface area (MSA) of SAPO-34 and SO_4^{2-}/TiO_2 catalysts have been identified as key parameters governing CO_2 desorption rate and heat consumption,[21] whereas the enhanced performance of $SO_4^{2-}/ZrTiO_x$ composite oxides has been primarily ascribed to their high acid site density.[22] Research on Al–FeOOH composite catalysts has also listed mesoporous surface area and the B/L acid ratio as the primary structure–activity correlation factors.[19] These metrics are all static, bulk characterization parameters. The spatial distribution of acid sites has received extensive attention. Previous studies have found that the distribution of acid sites at the single-particle scale is directly correlated with local catalytic performance.[23] This concept has been extended to CO_2 capture: defect-induced superstrong acid sites in core–shell nanocatalysts reduce the energy consumption of capture; the spatial synergistic effect of B/L acid sites in hierarchically structured Hβ-zeolites reduces the regeneration energy consumption by 44.1%.[24,25] However, the aforementioned designs are each optimized for a single temperature window. Meanwhile, existing studies generally conduct catalyst design and evaluation under fixed high-temperature desorption conditions (90–120 °C). For instance, the evaluation of the Fe-HZSM-5 catalyst at 96 °C demonstrated a 161% increase in the maximum desorption rate compared to the blank control;[13] similarly, the performance of the SnO_2/ATP catalyst was assessed at 88 °C.[26] Consequently, the acid strength and thermal response characteristics of different acidic functional groups vary significantly, and their catalytic contributions change dynamically with temperature.[27]

Previous studies have indicated that acid sites exhibit a functional dichotomy in amine regeneration: weak acid sites (such as hydroxyl groups on ZrO_xH_y) stabilize intermediates *via* hydrogen bonding at moderate temperatures,[12] whereas strong acid sites, including sulfonated MOF-derived superacids, redox-tunable Brønsted acids, and nickel single-atom catalysts, facilitate carbamate C–N bond cleavage and CO_2 release through proton supply, PCET, or direct electrochemical reduction pathways.[19,28,29] This temperature and energy-dependent division of labor essentially requires the spatial decoupling of functionally complementary but thermally mismatched sites to achieve hierarchical activation of energy across the entire capture process, wherein low-grade thermal energy drives proton transfer during the absorption stage and high-grade energy triggers bond cleavage during the desorption stage; this requirement cannot be met when these sites are homogeneously distributed on the same surface.[30]

To address these issues, this study proposes an interfacial regulation strategy based on spatial partitioning of the carbon-based catalyst surface, constructing bifunctional catalytic microdomains that integrate sulfonic acid groups ($-SO_3H$) and silanol hydrogen-bond networks (SiO_x–OH) (Fig. 1a). By leveraging the intrinsic differences in acid strength and thermal response characteristics between these two functional groups, temperature-adaptive synergistic catalysis is achieved.[31] At low temperatures, Si–OH groups dominate intermediate stabilization and proton pre-activation, while at high temperatures, $-SO_3H$ groups release protons to drive C–N bond cleavage. The proximal spatial distribution of these groups forms a proton relay channel, enabling segmented reaction activation and energy cascade matching throughout the absorption–desorption cycle (Fig. 1b). Combining *in situ* infrared characterization with DFT theoretical calculations, this work elucidates a dual-pathway desorption mechanism involving the coexistence of interfacial HCO_3^- decomposition and direct liquid-phase $MEACOO^-$ decomposition, thereby verifying the existence of a dual-proton transfer catalytic pathway.[32,33] Experimental results demonstrate that the optimized catalyst significantly enhances desorption efficiency and reduces regeneration energy consumption under simulated industrial conditions, while exhibiting excellent cyclic stability. This study elucidates the temperature-adaptive synergistic mechanism between strong and weak acid sites, providing a new theoretical basis for the design of low-energy-consumption catalytic materials for carbon capture.

2. Results and discussion

2.1 Design strategy and structural characteristics

Based on conventional amine-based CO_2 capture systems (Fig. S2), this study aims to investigate how cooperative surface groups on catalysts enhance CO_2 capture and explore interfacial mechanisms. Thus, the CO_2 absorption–desorption reaction process is facilitated by controlling the spatial distribution of surface functional groups within interfacial micro-regions of catalysts (Fig. 2a). The catalyst surface structure modulation strategy, termed the partial coating method, synergistically modulates both sulfonic acid ($-SO_3H$) and silicon functionality (SiO_x–OH).[34] By introducing the SiO_x–OH coating as the reactive site, followed by subsequent $-SO_3H$ group incorporation, surface acidity is synergistically enhanced.[35,36] Precise control of tetraethyl orthosilicate (TEOS) concentration enables engineered regulation of SiO_x–OH shell thickness and spatial exposure degree of $-SO_3H$ groups.[37]

As shown in Fig. 2a, the carbon(C)-coated Cu particle catalyst (Cu@C) was synthesized by a one-step hydrothermal method. The nomenclature follows the core–shell-functionalization order: Cu@C denotes a core–shell structure in which a copper core is encapsulated by a carbon shell; the terms in parentheses denote the grafting order of $-SO_3H$ (designated as S) and SiO_x–OH (designated as Si) onto the carbon shell; "T" denotes total coating using TEOS. The material prepared *via* sulfonation followed by thick SiO_x coating (Cu@C@(S–TSi)) (105 nm, Fig. S3) exhibits restricted proton transfer efficiency in internal active groups due to spatial hindrance limiting the

 This journal is © The Royal Society of Chemistry 2026

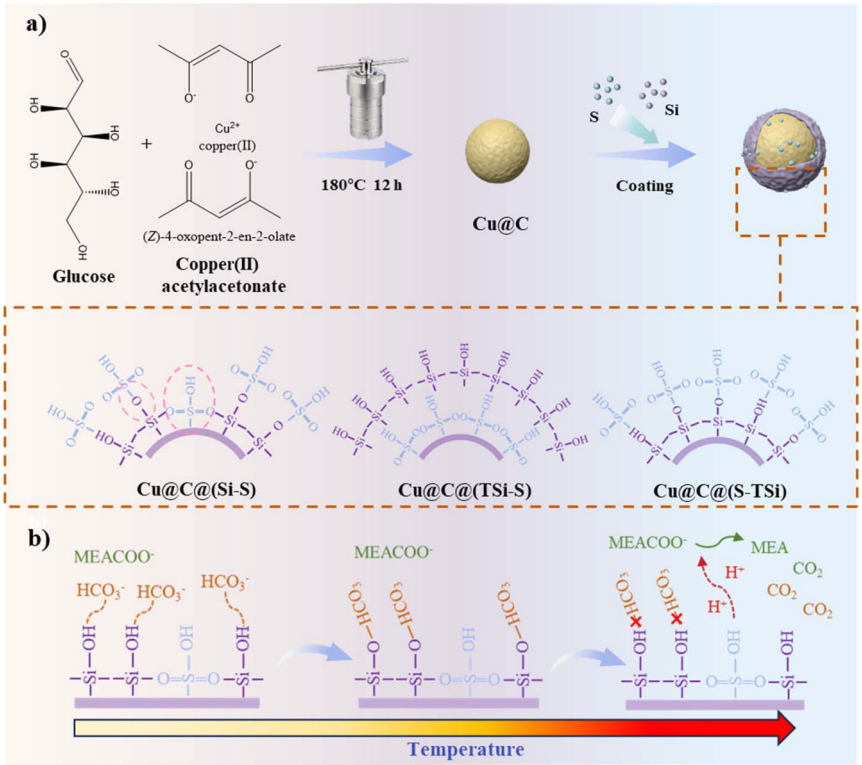


Fig. 1 (a) Schematic diagram for regulating the organic–inorganic interface effect on the catalyst surface. (b) Surface functional group response to the temperature gradient during CO_2 absorption–desorption.

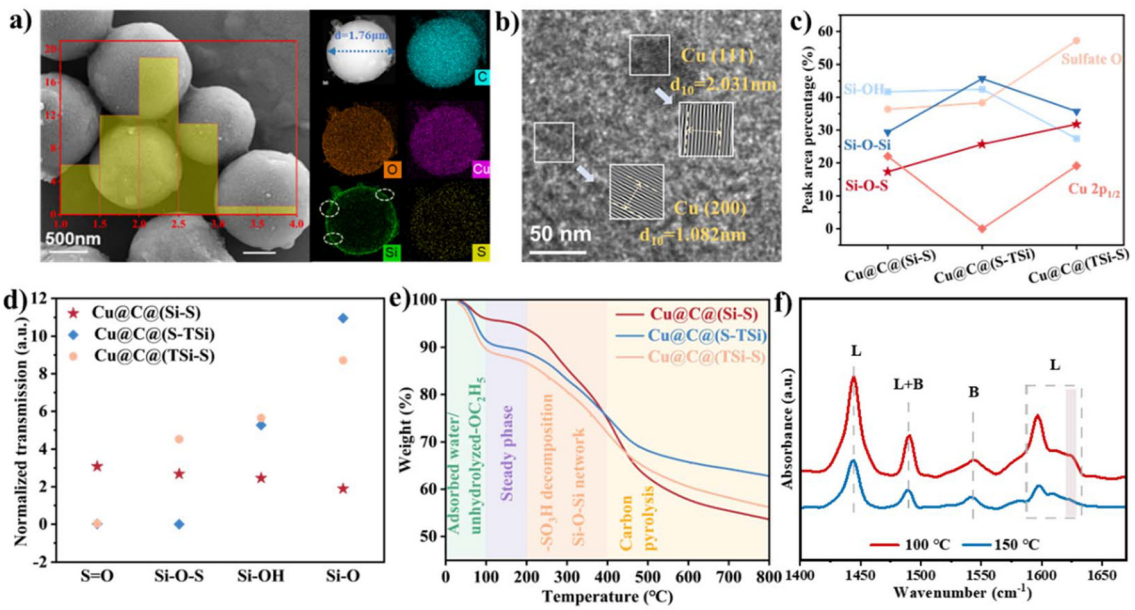


Fig. 2 (a) SEM and mapping images of Cu@C@(Si–S). (b) TEM image of Cu@C@(S–TSi). (c) Elemental compositions from XPS bonding state analysis across three catalysts. (d) Normalized FT-IR intensity plots for the three catalysts. (e) TGA results for Cu@C@(Si–S), Cu@C@(S–TSi), and Cu@C@(TSi–S). (f) Py-IR spectrum of Cu@C@(Si–S).

process. In contrast, the Cu@C catalyst prepared by thick SiO_x coating (102 nm) (Cu@C@(TSi–S)) after sulfonation (Fig. S4) shows dispersed surface $-SO_3H$ groups, while the thick shell blocks core functions. Notably, the Cu@C catalyst with sulfonation after thin SiO_x coating (18 nm) (Cu@C@(Si–S)) achieves controlled local shell cracking, fully utilizing synergy between

surface-dispersed –SO_3H groups and core functional groups. These structural variations systematically reveal correlations among impregnation sequences, acid site distribution, and defect engineering, establishing a structure–performance relationship model for optimizing catalytic CO_2 capture.

Scanning electron microscopy (SEM) images (Fig. 2a and S5) show size-varied microspheres composed of 2.2 μm particles, with structural details revealed by TEM (Fig. S6). High-angle annular dark-field (HAADF) elemental mapping performed in STEM (Fig. 2a and S7, S8) reveals a hierarchical layered structure comprising a Cu@C spherical core and silica-rich outer layers, directly confirming spatially separated active components achieved *via* controlled encapsulation. These hierarchical modifications, spanning from micrometer-scale morphology to nanoscale functional group distribution, could collectively establish optimized proton transfer pathways. High-resolution transmission electron microscopy (HRTEM) images (Fig. 2b) reveal a wide distribution of small crystalline domains with lattice fringes of 0.203 nm and 0.108 nm, corresponding to Cu (111) and Cu (200) planes. The 43° and 50° reflections in the X-ray diffraction (XRD) pattern confirm this assignment (Fig. S9a).

2.2 Characterization of the catalysts

To evaluate the surface chemical composition of distinct catalysts, X-ray photoelectron spectroscopy (XPS) analysis was employed. Fig. 2c schematically shows bond evolution in the materials, and the absence of Cu peaks on the Cu@C@(S–TSi) surface confirms complete SiO_x encapsulation. Conversely, thinner SiO_x coatings and surface defects formed after sulfonation result in stronger Cu signals detected in the other two materials. Verification of modularized surface composition is achieved through normalized FT-IR spectra (Fig. 2d), where functional group variations quantified in Fig. S10 reveal distinct bonding configurations dictated by synthetic methods. In Cu@C@(Si–S), the thin shell structure exerts a minimal shielding effect on sulfonic acid groups, resulting in the highest vibration intensity of the S═O bond (1394 cm^{-1}). The relatively weak signals of the Si–O bond (802 cm^{-1}) and Si–OH bond (958 cm^{-1}) further confirm the limited coverage of the silicon layer. In contrast, the thick-shelled Cu@C@(TSi–S) catalyst exhibits intensified Si–OH/Si–O vibrational signatures. Conversely, sulfur-related bonds remain undetected due to complete burial of pre-isolated –SO_3H groups beneath the thick silica layer. Compared with Cu@C@(TSi–S), Cu@C@(S–TSi) structure further demonstrates that interfacial Si–OH groups serve as bridges linking the –SO_3H groups.

To assess the thermal stability of surface functional groups of the materials, thermogravimetric analysis (TGA, Fig. 2e) was performed to confirm the thermal stability and distribution features of the surface species. The Cu@C@(Si–S) catalyst exhibits a 3 wt% mass loss below 100 °C, which was attributed to the removal of physisorbed water, while the other two materials show a 10 wt% loss due to volatilization of residual ethoxy groups (–OC_2H_5) from incomplete TEOS hydrolysis. Between 200 and 300 °C, all catalysts undergo 5–9 wt% mass reduction, driven by sulfonic acid group decomposition and Si–OH condensation into Si–O–Si networks. Carbon pyrolysis dominates mass loss above 400 °C. Notably, structural stability persists up to 200 °C, ensuring operational reliability during CO_2 absorption–desorption cycles, which typically operate below 100 °C in our systems.[35,36] To further assess the impact of –SO_3H and Si–OH groups on the catalyst's surface structure and functional performance, systematic pyridine-adsorption infrared spectroscopy (Py-IR) analyses were conducted. These interfacial bonding strategies integrate –SO_3H and Si–OH, as confirmed by Py-IR (Fig. 2f). The characteristic PyH^+ vibration at 1540 cm^{-1} indicates Brønsted acidity, while the coordinated pyridine bands at 1444–1633 cm^{-1} confirm Lewis acidity. The thermal treatment at 100–150 °C induces dehydration condensation of surface silanol groups (Si–OH) into a dense Si–O–Si network, thickening the silica shell and covering a substantial portion of the exposed Cu^{x+} species (Fig. S9b). This accounts for the 50% reduction in total acidity. Lewis acid sites, predominantly associated with the surface Cu^{x+}, exhibit higher thermal sensitivity than Brønsted sites, resulting in an increased B/L ratio from 0.32 to 0.35.

2.3 Catalytic CO_2 capture performance

The performance of the prepared catalysts in the integrated CO_2 capture process was evaluated by examining the CO_2 absorption capacity, as well as the amount and rate of CO_2 desorption in the MEA solution. The CO_2 absorption and desorption analyses were conducted by heating the CO_2-rich 30% MEA aqueous solution to 40 °C and 90 °C, respectively, in the presence of 0.0375 wt% of the catalyst. Previous studies indicate that complex hydrogen bonding networks in alkaline amine solutions hinder CO_2 desorption kinetics.[38,39] Synergistic interaction between Si–OH and –SO_3H groups as acid sites on catalyst surfaces modulates these networks, significantly enhancing desorption kinetics.

The interfacial dual-site synergy mechanism increases CO_2 desorption capacity by 44.35% compared to the control while boosting desorption efficiency by 8.62% (Fig. 3b and S11). The mechanism originates from normalized static FTIR spectra (Fig. 2d), where balanced surface functional group distribution facilitates proton-transfer channels and provides accessible pathways for HCO_3^- and H^+ adsorption. Crucially, hydroxyl (–OH) normalization results (Fig. 3b) reveal that Cu@C@(Si–S) possesses the highest surface –OH group density. These oxygen atoms form hydrogen bonds with H^+, accelerating proton migration in amine solutions. By optimizing proton-coupled reaction pathways, Cu@C@(Si–S) achieves 249.32% faster desorption kinetics than conventional systems (Fig. 3c). This originates from surface –OH groups anchoring protons *via* hydrogen bonds to create directional proton-transfer chains, significantly reducing migration barriers. Additionally, Cu@C@(Si–S) reduces energy consumption by 40% during the critical first 20 min of the desorption process (Fig. 3d). Durability tests through five consecutive CO_2 desorption cycles (Fig. 3e and f) demonstrate that heat-treated samples maintain superior cycling stability *versus* non-treated counterparts.

 This journal is © The Royal Society of Chemistry 2026

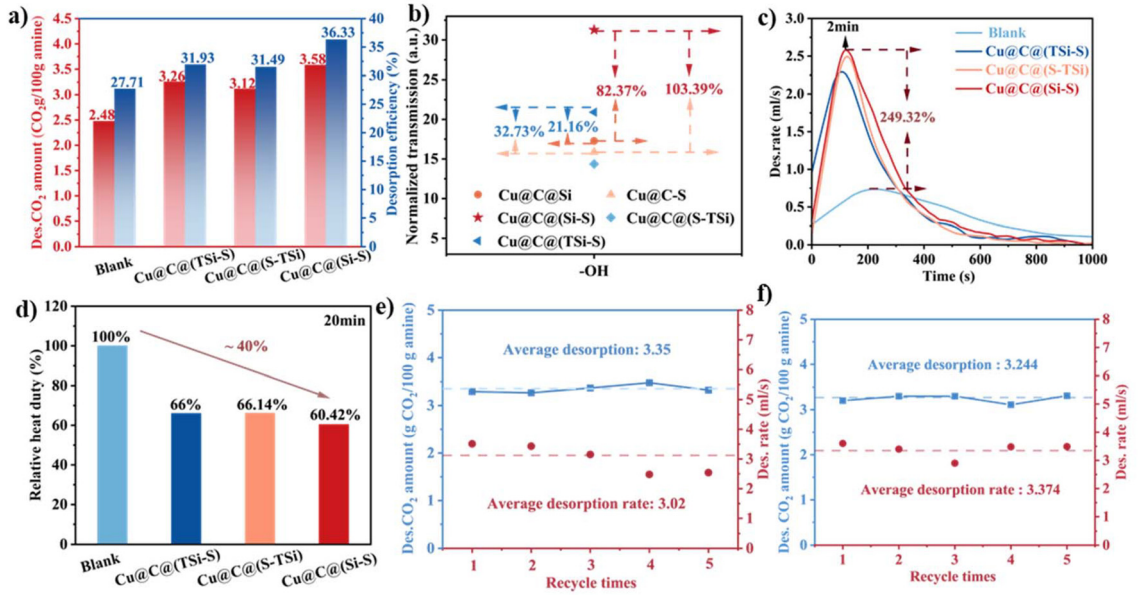


Fig. 3 (a) CO_2 desorption capacity and efficiency of the blank and catalytic systems. (b) Comparative hydroxyl (–OH) group variations among catalysts derived from normalized FT-IR analysis. (c) Desorption rate profiles, showing a 249.32% enhancement in peak rate (at 2 min) for catalysts *versus* the blank. (d) Relative thermal energy consumption during 20 min desorption cycles for blank and catalytic systems. The energy consumption was calculated from electricity meter readings, which involves heat losses and thus only the relative reduction compared to the blank run is reported. (e) Cyclic desorption performance of Cu@C@(Si–S) over 5 cycles (average capacity: 3.35; rate: 3.02). (f) Desorption stability of Cu@C@(Si–S) after 300 °C thermal treatment in an Ar–H_2 atmosphere over 5 cycles (average capacity: 3.244; rate: 3.374).

As shown in Fig. S13 and S14, all three catalysts exhibited catalytic effects throughout the CO_2 absorption–desorption cycle in the MDEA system, with Cu@C@(S–TSi) demonstrating the best overall performance. This phenomenon is primarily attributed to the difference in chemical environment between the MEA and MDEA systems. In the strongly alkaline MEA solution (pH ≈ 11.98), a large fraction of the surface Si–OH groups are converted to Si–O^-, which disrupts the continuity of the hydrogen-bond network and weakens the proton preorganization capability. In contrast, under the milder alkaline conditions of the MDEA system (pH ≈ 11.03), the Si–OH groups remain largely intact and can form a continuous hydrogen-bond network on the carrier surface, significantly enhancing interfacial CO_2 adsorption and accelerating mass transfer, thereby improving the overall catalytic efficiency.

To distinguish the respective roles of the two functional groups and to exclude interference from the Cu core, control experiments were conducted under identical conditions using the Cu-free catalysts C@Si (bearing only silanol groups) and C@S (bearing only sulfonic acid groups). As shown in Fig. S14, during the absorption phase, C@Si exhibited a significantly higher CO_2 uptake than C@S, whereas the trend was reversed during the desorption phase, where C@S outperformed C@Si. This pronounced temperature-dependent behavior clearly indicates that Si–OH dominates the absorption phase by stabilizing intermediates and preorganizing protons through hydrogen bonding, whereas –SO_3H governs the desorption phase by releasing protons to drive C–N bond cleavage and CO_2 release. The inferior desorption performance of C@Si confirms the strong adsorption of HCO_3^- on Si–OH sites, and DFT calculations further demonstrate that the adsorption energy of −0.48 eV renders the release kinetics unfavorable in the absence of sulfonic acid sites.

Notably, the exposed Cu^+ species can serve as Lewis acid sites, as confirmed by XPS Cu 2p spectra and Py-IR analysis. The intensities of the Cu 2p signals for the three catalysts differed significantly; Cu@C@(Si–S) exhibited the strongest signal due to the highest degree of Cu exposure resulting from local shell cracking induced by thin SiO_x coating and sulfonation, whereas Cu@C@(S–TSi) showed the weakest signal owing to complete encapsulation by thick SiO_x. Py-IR spectroscopy further indicated that thermally induced condensation of Si–OH groups covered these Cu species, leading to a decrease in Lewis acidity, thereby confirming that the Lewis acid sites originated from the exposed Cu species. Consequently, the Cu core primarily provides Lewis acid sites, which act synergistically with the Brønsted acid sites of –SO_3H groups and Si–OH to constitute a L/B acid cooperative catalytic system that facilitates CO_2 desorption. Furthermore, the cycling desorption stability of Cu@C@S without SiO_x–OH protection was evaluated over four cycles (Fig. S14). The results showed that the desorption performance declined significantly after the first cycle and subsequently stabilized at a lower level. This attenuation is attributed to the gradual loss of surface –SO_3H groups during cycling, with the exposed Cu@C surface becoming the dominant active component in subsequent cycles. In contrast, in the Cu@C@(Si–S) catalyst, the Si–OH network serves as an anchoring bridge, effectively preventing the detachment of

–SO_3H groups and maintaining stable catalytic activity over multiple cycles. This stabilizing effect is further supported by DFT calculations, which reveal a strong binding affinity between –SO_3H and the SiO_x–OH network, confirming the role of Si–OH as both a structural and functional bridge that immobilizes sulfonic acid sites and sustains long-term catalytic performance.

In the CO_2 absorption–desorption testing, in order to reveal the influence mechanism of the catalytic system on CO_2 mass transfer and reaction kinetics, this study analyzes the enhancement factor (E_i) in the absorption process and the activation energy (E_a) in the desorption process. The enhancement factor (E_i) represents the ratio of the mass transfer coefficient with chemical reaction to that with pure physical absorption.[40] It demonstrates the enhancement of mass transfer by reaction kinetics in chemical absorption processes. In the MEA-CO_2 absorption system, the reaction rate constant ($k_{reaction}$) increases significantly with temperature, leading to higher E_i (Fig. 4a). However, according to Henry's law, elevated temperature reduces CO_2 physical solubility. Thus, considering practical operation requirements, 40 °C was selected as the optimal absorption temperature in this study. To further examine the effect of desorption temperature on the catalytic process, the reaction activation energy (E_a) was calculated from Arrhenius plots by varying desorption temperatures in both blank and catalytic systems.[41] The catalytic process exhibited a significantly lower E_a value (35.07 kJ mol^{-1}) compared to the blank system (79.24 kJ mol^{-1}; Fig. 4b and S12), as derived from the Arrhenius equation. This reduced activation energy can directly facilitate carbamate decomposition and CO_2 desorption, highlighting the catalyst's role in lowering energy barriers for solvent regeneration.

Subsequent screening experiments involving modifications of four functional groups (Fig. 4c) were designed to evaluate their CO_2 desorption capacity and rate at 90 °C. Among the four functional group-modified catalysts, the SiO_x–OH and –SO_3H modified Cu@C catalyst exhibited the highest desorption efficiency and rate retention. Finally, a radar chart analysis (Fig. 4d) comprehensively compared the proposed catalyst with state-of-the-art materials MOFs, ionic liquids, and bimetallic composites across five critical metrics of technical maturity, cost, desorption rate, capture efficiency, and energy savings (Table S5). Table S5 lists the raw data for each indicator. For positive indicators (capture efficiency, desorption rate), higher values correspond to higher radar scores; for negative indicators (cost, energy consumption), lower values correspond to higher scores. All indicators are normalized to the 0–1 range by Min–Max normalization. Unlike the scalability constraints of MOFs, the mass transfer limitations in ionic liquids, and the cost inefficiencies of bimetallic materials, our carbon-based catalyst achieves industrial viability through simplified synthesis and superior desorption kinetics. Overall, the

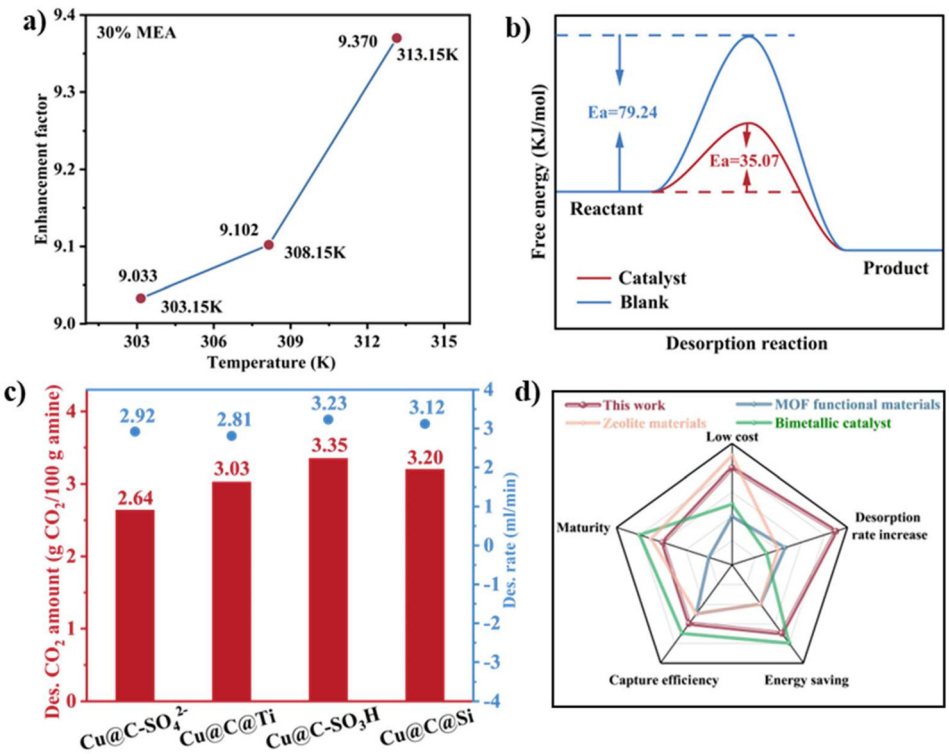


Fig. 4 (a) CO_2 absorption enhancement factors at various temperatures. (b) Comparison of desorption activation energies between blank and catalytic systems. (c) Performance comparison of surface-adsorbed functional groups screened on identical substrates. (d) Comparative analysis of cost efficiency, technological maturity, capture efficacy, energy savings, and desorption rate enhancement between reported catalysts and the proposed system.

This journal is © The Royal Society of Chemistry 2026

biomass-derived catalyst dominates in desorption rate, energy efficiency, and technical feasibility while maintaining competitive capture efficiency and cost-effectiveness.

2.4 *In situ* FT-IR analysis of catalytic CO_2 desorption

Traditional amine-based CO_2 desorption studies primarily focus on liquid-phase, thermally driven $MEACOO^-$ decomposition kinetics while overlooking interfacial species transport dynamics at catalyst surfaces. In the liquid bulk phase, $MEACOO^-$ undergoes thermal decomposition *via* a homogeneous pathway, whereas HCO_3^- at the interface is catalytically decomposed *via* a heterogeneous pathway on Si–OH and $-SO_3H$ sites. This spatial separation of the two pathways constitutes the dual-pathway mechanism proposed in this work, wherein their synergy lowers the energy barrier for CO_2 desorption.

To elucidate liquid-phase catalytic mechanisms, the dynamic behavior of the Cu@C@(Si–S) catalyst during CO_2 adsorption–desorption processes was investigated using Raman spectroscopy. Raman spectra of MEA solutions with and without the catalyst were compared at 30 minutes during CO_2 absorption and desorption. Three distinct peaks were observed at 1021, 1068, and 1157 cm^{-1}, assigned to the C–OH stretching of HCO_3^-, symmetric C–O stretching of CO_3^{2-}, and C–N stretching, respectively (Fig. 5a and b). Notably, the peak intensities of HCO_3^-, CO_3^{2-}, and $MEACOO^-$ exhibited significant enhancement during catalytic CO_2 absorption but diminished during desorption. The incorporation of the catalyst simultaneously accelerates the formation and decomposition of HCO_3^-, CO_3^{2-}, and $MEACOO^-$, with predominant enhancement of $MEACOO^-$ decomposition in amine solutions. These findings indicate that the liquid-phase environment is dominated by the decomposition pathway of $MEACOO^-$, whereas HCO_3^- mainly functions as a proton transfer medium and dynamic buffer.

Compared to liquid-phase reactions, this study used *in situ* infrared spectroscopy to confirm the existence of two catalytic desorption pathways at the interface (experimental details in S4). Spectral results revealed that HCO_3^- (~1635 cm^{-1}) exhibited the most significant dynamic changes, while $MEACOO^-$ (~1442/1428 cm^{-1}) and $MEAH^+$ (~1103/1162 cm^{-1}) showed weaker responses (Fig. 5c and e). This is because large-sized $MEACOO^-$ and $MEAH^+$ are less likely to exist in the confined interfacial regions, whereas small-sized HCO_3^- can be efficiently adsorbed and accumulate at the interface. Fig. 5c and d indicate that in the blank system below 80 °C, the concentration of HCO_3^- increased steadily due to the reverse reaction occurring as HCO_3^- was not saturated. The rise in the CO_2 peak might be attributed to the partial release of physically dissolved CO_2 during heating. When the temperature was raised above 80 °C, the forward reaction of HCO_3^- decomposition increased, leading to an increase in CO_2 production and a decrease in the peak intensity of HCO_3^-. Meanwhile, the peak intensities of $MEACOO^-$ and $MEAH^+$ slightly decreased,

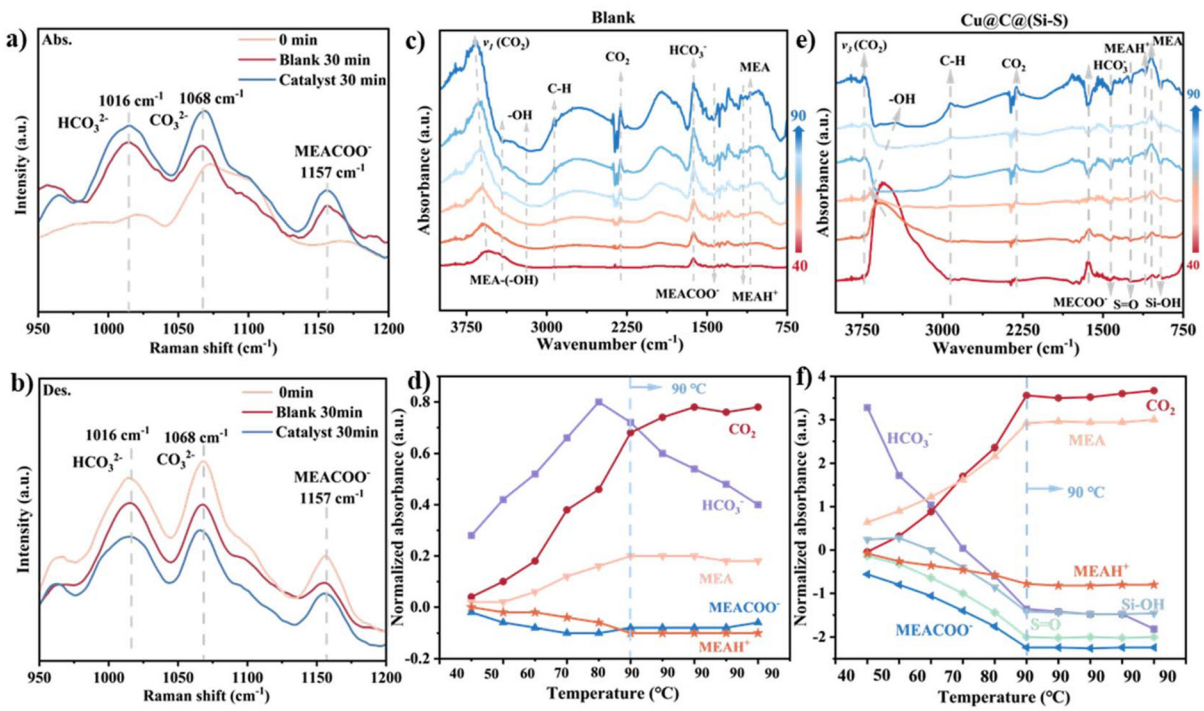


Fig. 5 (a and b) Time-resolved Raman spectra monitoring interfacial species evolution during catalytic (a) CO_2 absorption and (b) desorption processes. *In situ* FT-IR spectra (with subtraction of the time-0 spectrum) recorded during CO_2 desorption from a 30% CO_2-loaded MEA aqueous solution, with (c) the blank and (e) the catalyst, at temperatures ranging from 40 to 90 °C. (d and f) The normalized intensity of the FTIR peaks of the reaction-involved species with/without the Cu@C@(Si–S) catalyst.

suggesting a dual desorption mechanism dominated by HCO_3^- decomposition with minor contributions from $MEACOO^-$ decomposition. Additionally, the vibration at ~2927 cm^{-1} was attributed to the C–H stretching of MEA during regeneration, while the broad peak in the 3000–3700 cm^{-1} range could be deconvoluted into peaks at ~3417 and 3183 cm^{-1}, corresponding to the –OH groups of MEA and H_2O, respectively. The peak at 3600 cm^{-1} exhibited a blue shift, which was attributed to changes in environmental polarity or intermolecular interactions. In the presence of the catalyst, the broad peak in the 3000–3700 cm^{-1} range was ascribed to the –OH groups of either H_2O or MEA, and the peak at 3739 cm^{-1} was related to the ν_3 vibrational mode of CO_2.

2.5 Proton transfer in MEA regeneration

This study highlights how regulating reaction pathways at the catalyst interface drives a dual-mechanism decomposition dominated by HCO_3^- with $MEACOO^-$ assistance (Fig. 6a). Under reaction conditions, the Si–OH species facilitates the stabilization of intermediates by forming a hydrogen-bonding network in the aqueous environment, thereby promoting the electrostatic adsorption of HCO_3^- and $MEACOO^-$ ions onto the active interface. Concurrently, surface $-SO_3H$ groups directly donate protons to the hydroxyl oxygen in HCO_3^- and the carboxylate oxygen in $MEACOO^-$, cleaving the C–OH and C–N bonds to liberate CO_2. Partial Si^{3+}–OH polarizes adjacent water molecules, splitting O–H bonds to generate active H^+ and OH^-.[42] The dissociation-generated H^+ and OH^- form a localized charge difference at the interface region, facilitating proton migration and subsequent reactions. This interfacial –OH enrichment enhances proton mobility in organic solvents while $-SO_3^-$ continuously replenishes the proton storage. Concurrently, the Brønsted base $-SO_3^-$ extracts protons from H_2O and $MEAH^+$, reverting to acidic sites ($-SO_3H$) to sustain proton supply for desorption and regenerate MEA. Significant differences exist in the reaction pathways between the liquid bulk phase and the catalyst interface. In the liquid bulk phase, the thermal decomposition of $MEACOO^-$ is the dominant pathway, following conventional high-temperature decomposition routes. At the solid–liquid interface of the catalyst, HCO_3^- preferentially adsorbs onto Si–OH sites and decomposes at lower temperatures *via* a surface-mediated pathway. Due to the absence of microscopic enrichment zones in the solution, carbamate decomposes rapidly in the bulk phase. These results indicate that interface engineering plays a critical role in directing the CO_2 capture mechanism toward low-energy-consumption pathways, confirming that the dual-pathway mechanism originates from the spatial separation of bulk and interfacial reactions.

To further elucidate the desorption reaction pathway on the catalyst interface, DFT calculations were employed to evaluate the adsorption energies of key species at different functional sites.[43] As shown in Fig. 6b, the dual-acid surface exhibits strong adsorption affinity for HCO_3^- (−4.48 eV) but consider-

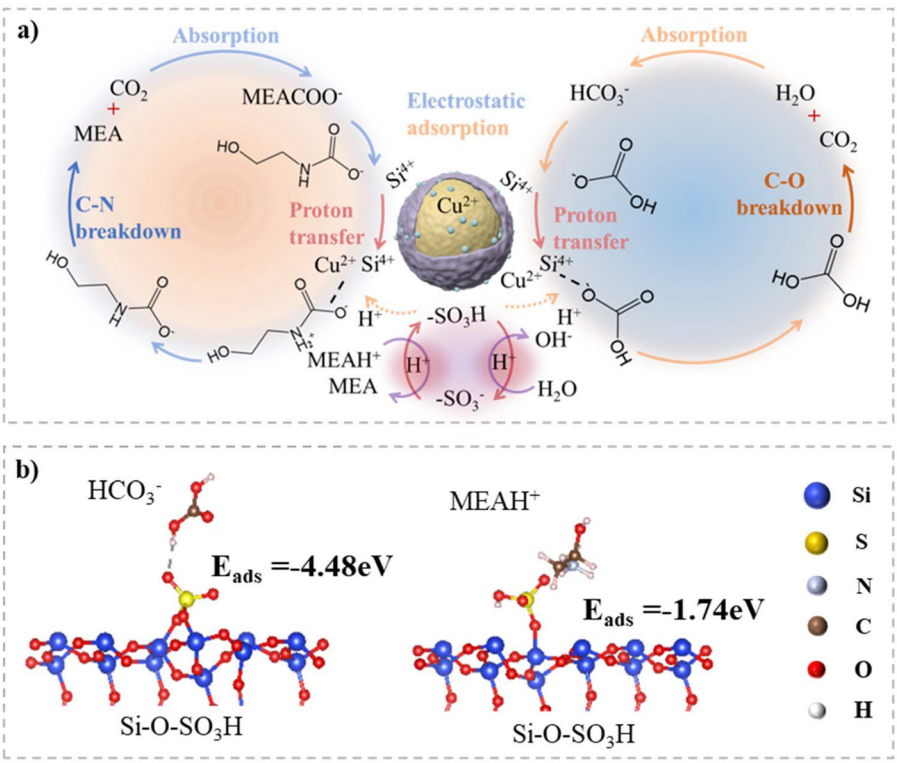


Fig. 6 Schematic illustration of the mechanism by which bifunctional groups promote CO_2 desorption in the liquid phase and at catalytic interfaces. (a) Reaction pathway schematic; (b) DFT adsorption energies at Si–O–SO_3H sites.

This journal is © The Royal Society of Chemistry 2026

ably weaker adsorption for $MEACOO^-$, indicating that HCO_3^- preferentially accumulates at the catalytic interface and participates in surface-mediated decomposition reactions, while $MEACOO^-$ mainly remains in the liquid phase and follows the conventional thermal decomposition pathway. In addition, the surface shows a moderate adsorption energy for $MEAH^+$ (−1.74 eV), suggesting that it can serve as a proton donor supplying protons to $-SO_3^-$ sites, thereby sustaining the proton cycle required for amine regeneration. Notably (Fig. S15), the isolated Si–OH site exhibits a stronger binding energy for HCO_3^- (−4.82 eV), confirming that it stabilizes bicarbonate species through hydrogen bonding and weak proton-donor interactions, thus facilitating CO_2 absorption. More importantly, the adsorption energy between Si–OH and $-SO_3H$ is −4.78 eV, indicating that Si–OH can serve as an anchoring bridge to stabilize surface $-SO_3H$ groups. Once this bridging structure is formed, the adsorption energy of the Si–O–SO_3H assembly toward HCO_3^- decreases to −4.48 eV, which is more favorable for the subsequent desorption of HCO_3^- compared with that of isolated Si–OH sites (−4.82 eV), thereby optimizing the desorption kinetics without sacrificing CO_2 capture capacity. The attenuation of the adsorption energy by 0.34 eV (from −4.82 eV for pure Si–OH to −4.48 eV for the Si–O–SO_3H dual-site configuration) holds significant mechanistic implications. This reduction precisely balances the conflicting requirements for low-temperature adsorption and high-temperature desorption: sufficient affinity is required to stabilize the HCO_3^- intermediate during low-temperature adsorption, whereas excessively strong adsorption would increase the desorption energy barrier and hinder CO_2 release during high-temperature desorption. Consequently, the Si–O–SO_3H dual-site configuration achieves a moderate adsorption strength that is neither too strong (which would cause product inhibition) nor too weak (which would fail to stabilize the intermediate), thereby providing atomic-scale guidelines for the rational design of bifunctional catalytic sites for CO_2 desorption. In summary, the Brønsted acidity of Si–OH modulates the activation of interfacial species through hydrogen bonding and weak proton transfer, whereas the strong proton-donating ability of $-SO_3H$ critically promotes the decomposition of carbamate and bicarbonate intermediates. The synergistic effect of these two functional groups, together with the structural stabilization provided by Si–OH bridging, effectively lowers the overall energy barrier for CO_2 desorption and significantly enhances the regeneration efficiency of amine-based capture systems.

2.6 Perspectives

Although the stability over five cycles and the thermal treatment data at 300 °C indicate that Cu@C@(Si–S) exhibits robustness under laboratory conditions, several practical issues must be addressed for real-world applications. (1) During long-term operation, thermally stable salts (such as sulfates and oxalates) and amine degradation byproducts may deposit on the catalyst surface, blocking $-SO_3H$ and SiO_x–OH sites. The catalyst's activity is expected to be restored through simple regeneration procedures, such as water washing or dilute acid washing. (2) The leaching of sulfonic acid groups under hydrothermal conditions is a known issue for this class of materials. Employing stronger anchoring strategies, for example, using aryl sulfonic acids with multiple attachment points or introducing cross-linked siloxane networks, can enhance the durability of the functional shell. (3) Actual flue gas contains SO_2, NO_x, and particulate matter, which may cause corrosion or irreversible poisoning of the catalyst. Upstream desulfurization and denitrification can mitigate this issue, while a protective porous coating (*e.g.*, silica or polymer) that permits CO_2 permeation but blocks larger acidic molecules can provide additional protection. Addressing these challenges is critical for advancing this catalytic system from laboratory studies to practical applications.

3. Conclusion

In summary, we have developed a carbon-based catalyst with a spatially hierarchical structure, in which surface-modified $-SO_3H$ and SiO_x–OH sites enable temperature-adaptive proton transfer for efficient CO_2 capture. This hierarchical design operates throughout the entire process: during the low-temperature absorption stage, Si–OH groups play a dominant role by stabilizing intermediates and pre-organizing protons *via* a hydrogen-bonding network; during the high-temperature desorption stage, $-SO_3H$ groups take over to release protons and drive C–N bond cleavage for CO_2 release. This division of labor is particularly pronounced in the weakly alkaline MDEA environment, where Si–OH groups remain intact. The spatial proximity of these two types of sites creates a proton relay channel that bridges the absorption and desorption stages, achieving energy-level hierarchical activation matched to the temperature profile of the entire process. Mechanistically, the interfacial pathway preferentially proceeds *via* HCO_3^- decomposition rather than direct $MEACOO^-$ cleavage, establishing a dual-pathway mechanism that lowers the overall desorption energy barrier. The strategy of sulfonation after thin-layer SiO_x coating anchors $-SO_3H$ groups onto the silanol network, ensuring long-term stability. In summary, this work demonstrates that spatially hierarchical site engineering on carbon-based nanomaterials provides a rational design principle spanning the entire CO_2 absorption–desorption process for energy-efficient amine regeneration.

Author contributions

Mengcheng Zhan: investigation, data curation, formal analysis, and writing – review & editing. Jingwen Jiang: investigation, experimental validation, and data analysis. Tingting Xia: material preparation, characterization testing, and writing – original draft. Jichao Hu: investigation. Weiping Zhang: supervision, project administration, and funding. Dong Xu: supervision and funding. Yulong Wang: supervision. Bingyuan Zeng: auxiliary experiments. Baohui Li: supervision. Dong Fu: super-

vision. Kun Zhao: conceptualization, funding acquisition, and writing – review & editing.

Conflicts of interest

The authors declare that they have no known competing financial interests or personal relationships that could have appeared to influence the work reported in this paper.

Data availability

All supporting data required to verify the conclusions are provided within the supplementary information (SI). Supplementary information is available. See DOI: https://doi.org/10.1039/d6nr03055f.

Raw experimental and computational datasets in a compressed zip archive are openly available in Zenodo at https://doi.org/10.5281/zenodo.22830743.

Acknowledgements

This work was supported by the Fundamental Research Funds for the Central Universities (2025MS158), the National Key Research and Development Project of China (2024YFE0110800, 2023YFC3708203), and the National Natural Science Foundation of China (42477411).

References

1 Y. Guo and T. A. Hatton, *Nat. Chem. Eng.*, 2025, **3**, 70–78.
2 W. Xie, B. Li, L. Liu, H. Li, M. Yue, Q. Niu, S. Liang, X. Shao, H. Lee, J. Y. Lee, M. Shao, Q. Wang, D. O'Hare and H. He, *Chem. Soc. Rev.*, 2025, **54**, 898–959.
3 J. Z. Y. Tan, J. M. Uratani, S. Griffiths, J. M. Andresen and M. M. Maroto-Valer, *Nat. Rev. Chem.*, 2025, **9**, 656–671.
4 H. Chen, H. Zhang, Z. Yan, Z. Zhang, L. Tong, J. Yang, X. Li, Y. Wang and S. Saheed, *Sep. Purif. Technol.*, 2025, **378**, 134755.
5 M. Dai, R. Wang, N. Sun, W. Wei and X. Chen, *ChemCatChem*, 2026, **18**, e01827.
6 U. H. Bhatti, A. K. Shah, J. N. Kim, J. K. You, S. H. Choi, D. H. Lim, S. Nam, Y. H. Park and I. H. Baek, *ACS Sustainable Chem. Eng.*, 2017, **5**, 5862–5868.
7 Z. Zheng, Y. Wang, M. Wang, G. Zhao, G. Hao and A. Lu, *Nat. Commun.*, 2024, **15**, 8919.
8 S. Zhang, Y. Liu, Y. Huang, C. Wang, J. Mu, C. Zhang, D. Huang and C. Chen, *Commun. Chem.*, 2026, **9**, 167.
9 Q. Li, G. Wei, J. Qi, K. Zhao and B. Han, *Acc. Chem. Res.*, 2025, **58**, 3111–3122.
10 Z. Geng, Y. Yang, Y. Wang, W. Xu and T. Zhu, *Environ. Sci. Technol. Lett.*, 2026, **13**, 220–226.
11 M. Imran-Shaukat, H. Haghani, R. Apaiyakul, H. Gao, Z. Liang, P. Tontiwachwuthikul and T. Sema, *Sep. Purif. Technol.*, 2025, **359**, 130434.
12 C. Zhou, M. T. Beydokhti, F. Rammal, P. Kumar, M. Lacroix, W. Vermeiren, M. Dusselier, Y. Liao and B. F. Sels, *Nat. Catal.*, 2025, **8**, 270–281.
13 B. Wang, W. Han, F. Dong, H. Feng and Z. Tang, *Mol. Catal.*, 2026, **592**, 115736.
14 A. Ibrahim, M. Imran-Shaukat, B. Liu, M. Xiao, H. Gao, Z. Liang, P. Tontiwachwuthikul and T. Sema, *J. Environ. Chem. Eng.*, 2026, **14**, 123271.
15 Q. Sun, T. Li, Y. Mao, H. Gao, T. Sema, S. Wang, L. Liu and Z. Liang, *Ind. Eng. Chem. Res.*, 2021, **60**, 18304–18315.
16 Y. Li, L. Xing, Z. Chen, G. Zhan, B. Yuan, Y. Peng, L. Wang and J. Li, *Appl. Catal., B*, 2024, **358**, 124350.
17 S. Zhao, D. Wang, R. Amal and L. Dai, *Adv. Mater.*, 2019, **31**, 1801526.
18 H. Wang, T. Yang, J. Wang, Z. Zhou, Z. Pei and S. Zhao, *Chem*, 2024, **10**, 48–85.
19 X. Li, C. B. Musgrave, A. Liu, J. Meng, J. Zhang, W. A. Goddard and Y. Liu, *Nat. Commun.*, 2025, **16**, 4339.
20 Z. Liu, C. Fu, T. Qi, H. Zhou, G. Hao, Y. Guo and G. Hu, *Carbon Energy*, 2026, e70229.
21 X. Zhang, X. Zhang, H. Liu, W. Li, M. Xiao, H. Gao and Z. Liang, *Appl. Energy*, 2017, **202**, 673–684.
22 Z. Geng, Y. Yang, Y. Wang, T. Zhu and W. Xu, *Sep. Purif. Technol.*, 2023, **327**, 124889.
23 T. T. Le, A. Chawla and J. D. Rimer, *J. Catal.*, 2020, **391**, 56–68.
24 M. S. Alivand, O. Mazaheri, Y. Wu, A. Zavabeti, A. J. Christofferson, N. Meftahi, S. P. Russo, G. W. Stevens, C. A. Scholes and K. A. Mumford, *Nat. Commun.*, 2022, **13**, 1249.
25 Z. Zheng, Q. Sun, H. Gao and Z. Liang, *Fuel*, 2026, **416**, 138591.
26 Z. Tan, S. Zhang, F. Zhao, R. Zhang, F. Tang, K. You, H. Luo and X. Zhang, *Chem. Eng. J.*, 2023, **453**, 139801.
27 W. Srisang, F. Pouryousefi, P. A. Osei, B. Decardi-Nelson, A. Akachuku, P. Tontiwachwuthikul and R. Idem, *Chem. Eng. Sci.*, 2017, **170**, 48–57.
28 M. S. Alivand, O. Mazaheri, Y. Wu, A. Zavabeti, A. J. Christofferson, N. Meftahi, S. P. Russo, G. W. Stevens, C. A. Scholes and K. A. Mumford, *Nat. Commun.*, 2022, **13**, 1249.
29 P. Li, Y. Mao, H. Shin, Q. Yang, X. Cheng, Y. Li, K. Li, H. Yu, R. Mulder, W. K. Pang, H. Jin, Y. Zhao, Z. Zheng, E. Finch, K. Hearn, B. Jia, G. I. N. Waterhouse, Z. Wang and T. Ma, *Nat. Energy*, 2025, **10**, 1262–1273.
30 Y. Niu, S. Zou, A. H. Bhatti, M. Waris, C. Li, M. S. Alivand, F. Barzagli, K. A. Mumford, H. Zhou and R. Zhang, *Chem. Eng. J.*, 2025, **526**, 171282.
31 U. H. Bhatti, *Energy Fuels*, 2026, **40**, 9803–9812.
32 L. Liang, W. Kong, Z. Dong, X. Zhong, T. Song, T. Wang, M. Fang, W. Li and S. Li, *J. Cleaner Prod*, 2025, **521**, 146218.
33 J. Xiong, Q. Sun, L. Ke, S. Wang, Z. Wang, H. Gao, Z. Liang and Y. Mao, *J. Energy Chem.*, 2026, **115**, 326–336.

 This journal is © The Royal Society of Chemistry 2026

34 J. Jiang, Y. Wang, Y. Li, J. Huang, W. Zhang, D. Wang, D. Xu, D. Fu, P. Zhang, L. Wang and K. Zhao, *Bioresour. Technol.*, 2026, **443**, 133789.
35 U. H. Bhatti, M. S. Alivand, F. Barzagli, M. G. Sanku, J. Gascon and K. A. Mumford, *ACS Sustainable Chem. Eng.*, 2023, **11**, 11955–11964.
36 Z. Zheng, Q. Sun, H. Gao and Z. Liang, *Fuel*, 2026, **416**, 138591.
37 Y. S. Kim and G. S. An, *Ceram. Interfaces*, 2025, **51**, 379–385.
38 J. Jo, J. Park, S. Kwon, M. Park, J. Jung, Y. Yoo and D. Kang, *J. Environ. Chem. Eng.*, 2023, **11**, 110108.
39 J. Kim, K. Kim, H. Lim, J. H. Kang, H. S. Park, J. Park and H. Song, *J. Environ. Chem. Eng.*, 2024, **12**, 112664.
40 J. Jiang, B. Zhao, Y. Zhuo and S. Wang, *Int. J. Greenhouse Gas Control*, 2014, **29**, 135–141.
41 M. Li, L. Xing, Z. Xu, Z. Liang, T. Qi, Y. Li, S. Zhang and L. Wang, *Environ. Sci. Technol.*, 2023, **57**, 15465–15474.
42 Y. D. Kim, T. Wei, J. Stultz and D. W. Goodman, Dissociation of Water on a Flat, Ordered Silica Surface, *Langmuir*, 2003, **19**(4), 1140–1142.
43 Y. Zhao, K. Zhao, C. Hu, X. Guo, P. Du, D. Xu, W. Zhang, L. Qi, P. Zhang, C. Sun, B. Zeng, L. Li, S. Du, L. Wang and D. Fu, *Carbon Energy*, 2026, e70304.

This journal is © The Royal Society of Chemistry 2026